



Atomically dispersed Mo atoms on amorphous g-C₃N₄ promotes visible-light absorption and charge carriers transfer

Ruiyang Zhang^{a,1}, Penghui Li^{a,1}, Fang Wang^a, Liqun Ye^{b,*}, Abhijeet Gaur^c, Zeai Huang^a, Ziyan Zhao^a, Yang Bai^a, Ying Zhou^{a,*}

^a State Key Laboratory of Oil and Gas Reservoir Geology and Exploitation, School of Materials Science and Engineering, Southwest Petroleum University, Chengdu, 610500, China

^b Engineering Technology Research Center of Henan Province for Solar Catalysis, Collaborative Innovation Center of Water Security for Water Source Region of Mid-line of South-to-North Diversion Project of Henan Province, Nanyang Normal University, Nanyang, 473061, China

^c Institute for Chemical Technology and Polymer Chemistry, Karlsruhe Institute of Technology, Karlsruhe, 76131, Germany



ARTICLE INFO

Keywords:

Amorphous Mo/C₃N₄
Atomically dispersed Mo atoms
Amorphous transformation
Photocatalysis
CO₂ reduction

ABSTRACT

Atomically dispersed atom catalysts with atomically distributed active metal centers have attracted great attention owing to the maximum atom efficiency and excellent selectivity. Herein, for the first time, we found atomically dispersed Mo atoms can be formed on g-C₃N₄, and induce its amorphous transformation. This amorphous transformation leads to the formation of strong band tails with remarkably enhancing the absorbance edge of Mo-C₃N₄ up to 750 nm, resulting in almost whole visible-light range absorption. The formation of new Mo-C and Mo-N bonds due to strong interfacial interaction between atomically dispersed Mo atoms and g-C₃N₄ provide new electron and hole transport pathways to accelerate the separation of charge carriers. As a result, amorphous Mo/C₃N₄ (a-Mo/C₃N₄) reveals excellent photoreduction of CO₂, yielding CO and H₂ productions of 18 and 37 μmol g⁻¹ h⁻¹ under visible-light illumination ($\lambda > 420$ nm), which manifest a remarkable 10.6- and 4-folds enhancement of that over crystalline g-C₃N₄. This finding provides a conceptually different approach to fabricate high-efficient photocatalyst through the strong interfacial interaction between atomically dispersed metal atoms and host.

1. Introduction

Photocatalysis has emerged as a research focus in the field of environment and energy owing to its great potential to realize zero-carbon emission to improve the human lives of future generations [1–6]. To this end, developing efficient photocatalyst with strong visible-light response and fast charge carriers transfer is a challenging yet urgently needed work [7,8]. To improve the visible-light response, the fabrication of amorphous semiconductors has attracted great attention [9–14]. Theoretical calculations and experiments have confirmed that amorphous semiconductors usually possess much smaller bandgap than their crystalline phase originated from their strong band tails [15]. However, owing to the lack of long-range order, amorphous semiconductors usually suffer from the rapid recombination of photogenerated charge carriers, hindering the photocatalytic activity.

Recently, atomically dispersed atom catalysts with atomically distributed active metal centers have demonstrated maximum atom

efficiency and provided new electron transport pathways to suppress the recombination of charge carriers [16–19]. Several strategies have been developed for the fabrication of atomically dispersed atom catalysts. A common way is to use the interaction of metal and substrate to atomically anchor metal on the related support to form metal-support bonds [16]. However, to lead metal at a very low level (usually lower than 1%) is necessary to avoid large areas of metal agglomeration, which directly limits the application of atomically dispersed atom catalysts [17–19]. So far, it still remains a great challenge for the fabrication of atomically dispersed atom catalysts with a high level of loading amount. Additionally, most reports focus on the atomically dispersed atom itself, while the strong interfacial interaction between atom and substrate may induce remarkable structure changes even phase transformation, which is different from large particles that have no or little impact on the structure of substrate [20]. If the strong interfacial interaction between atomically dispersed atom and semiconductor host can realize the amorphous transformation of

* Corresponding authors.

E-mail addresses: yeliquny@163.com (L. Ye), yzhou@swpu.edu.cn (Y. Zhou).

¹ These authors contributed equally to this work.

photocatalyst, a synergistic effect may be achieved, in which the amorphous transformation provides a strong band tail to enhance the light absorption, while the new electron transport pathways between the atomically dispersed metal atoms and semiconductor host accelerate the separation of charge carriers. However, there are still no reports on the amorphous transformation induced by atomically dispersed metal atom due to the strong ionic bond and stable crystal structure of most metal-based semiconductors [21–23]. Graphitic carbon nitride ($g\text{-C}_3\text{N}_4$), a graphene analogues semiconductor, possesses weak van der Waals forces between layers as well as weak hydrogen bonding cohesion between polymeric melon units, but strong covalent C–N bonds in the melon units [9,24–27]. Therefore, the introduction of atomically dispersed metal atom could destroy the weak interlayer and planar cohesion but each melon units are still maintained, thus resulting in amorphous transformation of $g\text{-C}_3\text{N}_4$ [9].

Inspired by considerations above, we reported a conceptually different strategy for the fabrication of amorphous semiconductor induced by atomically dispersed metal atoms. Amorphous Mo– C_3N_4 (a-Mo/ C_3N_4) has been predicted via theoretical calculations and successfully prepared through facile pyrolysis of mixture of melamine and ammonium molybdate. Impressively, the introduction of atomically dispersed Mo atoms not only caused distorted crystal lattice and disordered atomic arrangement of $g\text{-C}_3\text{N}_4$ which led to a phase transition from crystalline to amorphous, but also created new bonds (Mo–C and Mo–N) which provided new electrons and holes transfer pathway to accelerate the separation of charge carriers. As a result, the obtained black a-Mo/ C_3N_4 reveals excellent photocatalytic efficiency for conversion of CO_2 , demonstrating its great potential in the application of clean energy production.

2. Experiments

2.1. Materials

Melamine ($\text{C}_3\text{H}_6\text{N}_6$, 99.99%) was purchased from Aladdin Chemical Reagent Corp. Ammonium molybdate ($(\text{NH}_4)_6\text{Mo}_7\text{O}_{24}\cdot 4\text{H}_2\text{O}$, 99%) was purchased from Chengdu Kelong Chemical Reagent Corp, PR China. High-purity milli-Q water was used in all experiments.

2.2. Preparation of a-Mo/ C_3N_4 photocatalyst

A-Mo/ C_3N_4 was synthesized via a facile polycondensation method. A typical preparation of the a-Mo/ C_3N_4 catalysts was as follows: a certain amount of $(\text{NH}_4)_6\text{Mo}_7\text{O}_{24}\cdot 4\text{H}_2\text{O}$ and 10 g of $\text{C}_3\text{H}_6\text{N}_6$ (Mo element/melamine molar percentage: 0–5%) was dissolved in 40 mL of deionized water. The solution was stirring for 2 h to obtain a homogeneous solution. The mixture was poured into Petri dishes to evaporate water at 60 °C. After being cooled, the obtained product was placed in a semi-closed porcelain boat with a cover to reduce sublimation. The porcelain boat was heated in the tube furnace at 550 °C in air atmosphere with a heating ramp of 10 °C/min. The temperature was kept at 550 °C for 4 h and then cooled to room temperature. Then, the obtained powders were ground and sieved to fine powders. For comparison, particle Mo/ $g\text{-C}_3\text{N}_4$ was fabricated through the pyrolysis of as-prepared $g\text{-C}_3\text{N}_4$ and ammonium molybdate.

2.3. Characterization

The structure and crystallinity of the samples were investigated by X-ray powder diffraction (XRD, PANalytical X'pert) with Cu K α radiation operated at 40 kV/40 mA. The Fourier-transform infrared (FTIR) spectra were performed on a Nicolet 6700 spectrometer on samples embedded in KBr pellets. Aberration-corrected high-angle annular dark field scanning transmission electron microscopy (HAADF-STEM) was conducted on a JEOL ARM200CF with a dual-type EDS detector (JED-2300 T). The N_2 sorption isotherm and Brunauer-Emmett-Teller (BET)

surface area were determined by the nitrogen adsorption method (Quadasorb SI). Inductively coupled plasma atomic emission spectroscopy (ICP-AES) was performed on an Agilent Icpoes 730. UV-vis DRS were recorded at room temperature on a Shimadzu UV-2600 spectrophotometer equipped with an integrating sphere using Ba_2SO_4 as the reflectance standard. X-ray photoelectron spectroscopy (XPS) measurements were performed using a Thermo ESCALAB250Xi X-ray photoelectron spectrometer and all of the binding energies were referenced to the C 1s level at 284.8 eV. The photoluminescence (PL) spectra were measured with a fluorescence spectrophotometer (F-7000, Japan). Time-resolved photoluminescence spectra were recorded on FLS920 fluorescence lifetime spectrophotometer (Edinburgh, Instruments, UK). The Mo K-edge X-ray absorption fine structure (XAFS) recorded in transmission mode at beamline BL14W1 with the Si (311) monochromator in Shanghai Synchrotron Radiation Facility (SSRF). The corresponding energy calibration was determined with the Mo metal foil, and S_0 was optimized at 0.92. The EXAFS data samples have been analyzed using the Athena and Artemis.

2.4. Photoelectrochemical test

Photoelectrochemical (PEC) measurements were conducted in a three-electrode system on a CH660D electrochemical work station, using the sample films as the working electrode, saturated calomel electrode (SCE) as the reference electrode, and Pt wire as the counter electrode. The experiment was employed at the 300 W xenon lamp with visible light filter (> 420 nm). The photocurrent-time and electrochemical impedance experiments for sample films at open circuit potential (OCV) were performed in 0.5 M Na_2SO_4 . For working electrodes, 0.2 g of the above obtained photocatalysts were ground together with 0.08 g of polyethylene glycol (molecular weight = 20000) and 2 mL of water to form a slurry. The slurry was coated on ITO glass with an active area of 4 cm^2 (film thickness: ca. 100 μm) subsequently treated at 180 °C for 2 h.

2.5. Photocatalytic performance test

The photocatalytic reduction activities for CO_2 conversion was done in closed gas system at ambient temperature and atmospheric pressure. Then 50 mg fine photocatalyst firstly dissolved in a petri dish with an area of 38.5 cm^2 paving with an appropriate amount of water, the petri dish is then placed in a vacuum drying oven at a temperature of 60 °C. Then the dried petri dish with water was put in mid-air of the reaction cell. Prior to the light irradiation, the above system was thoroughly vacuum-treated to remove the air completely, and then the CO_2 gases (99.999%) were filled in the reaction system of 380 mL. After that, the reactor was irradiated from the top by a 300 W Xe lamp with a cutoff filter ($\lambda > 420$ nm). During the irradiation, 1 mL of gas was taken from the reaction cell for subsequent qualitative analysis by GC9790II gas chromatography (GC, Tian Mei Analytical Instrument Co., Ltd., China) equipped with a thermal conductivity detector (TCD) and a flame ionization detector (FID, TXD-1). The quantification of the production yield was based on a calibration curve. The outlet gases were determined to be CO, CH_4 and H_2 .

2.6. Calculation methods

The first-principles density functional theory plus dispersion method implemented in the DMol³ package was used for all the calculations of the study. All the structures were fully optimized using the generalized gradient approximation (GGA), treated by the Perdew–Burke–Ernzerhof exchange–correlation potential (PBE) with long range dispersion correction via Grimme's scheme. An all electron double numerical atomic orbital augmented by d-polarization functions (DNPs) is used as the basis set. Geometry optimizations were performed with convergence thresholds of 0.002 ha \AA^{-1} on the max force, 0.005 \AA

on the displacement, and 1×10^{-5} ha on the energy. The self-consistent field (SCF) procedure was used with a 1.0^{-5} ha value. The Brillouin zones are sampled by $3 \times 3 \times 1$ k -points using the Monkhorst-Pack scheme. The bulk structure of g-C₃N₄ belongs to the hexagonal space group P-6M2. The optimized lattice constant of the bulk g-C₃N₄ is $a = b = 4.72$ and $c = 6.72$. The vacuum between the g-C₃N₄ (001) monolayers was 15 Å which is large enough to avoid interactions between periodic images. To investigate the geometric structure variations of monolayer g-C₃N₄ with the different atoms of Mo, 4×4 supercell of g-C₃N₄ (001) was employed. In addition, a 3×3 supercell of the g-C₃N₄ (001) monolayer was used for CO₂ reduction. Meanwhile, the LST/QST tools were employed to calculate the activation barrier energies (E_a) and transition states (TS) of CO₂ reduction paths.

3. Results and discussion

3.1. Synthesis and characterization

The geometric structure variations of monolayer g-C₃N₄ after the introduction of atomically dispersed Mo atoms was first investigated through the theoretical simulation (Fig. 1a and Table S1). The introduction of Mo atoms causes obvious outward twisting of melon units with the max shape variable of 4.10%, while the atomic coordination in each melon unit as well as the C–N–C coordination between two nearest neighboring melon units are still maintained. This result demonstrates that the long-range order of g-C₃N₄ is broken owing to the introduction of Mo atoms while the short-range order is still maintained, implying the phase transition from crystalline to amorphous.

To verify these theoretical predictions, a-Mo/C₃N₄ has been

successfully prepared by a facile pyrolysis of mixture of melamine and ammonium molybdate as shown in Scheme S1. The amount of Mo in the samples detected through inductively coupled plasma atomic emission spectroscopy (ICP-AES) is close to that of theoretical calculations (Fig. S1). Impressively, a remarkable color change from yellow to black was observed after the introduction of Mo atoms as shown in Fig. 1b, indicating the whole visible-light range absorption. The as-prepared a-Mo/C₃N₄ revealed various changes: (I) two typical diffraction peaks at 13.3° and 27.7° corresponding to the (100) and (002) planes of g-C₃N₄ [28,29] became weaker as the increasing amount of Mo atoms and disappeared when the Mo amount increased to 4%, indicating the long-range order of g-C₃N₄ has been broken (Fig. 1c). It should be noted that no obvious peak shifts were found among all amount of Mo, indicated that Mo was not merged into the lattice of g-C₃N₄; (II) the bands in FTIR spectrum at the range of 1200–1600 cm⁻¹ still exist (Fig. 1d), indicating the C–N heterocycles are maintained and the short-range order of g-C₃N₄ remains unchanged [30]; (III) the large sheets of g-C₃N₄ was destroyed into nano-scale pieces and no lattice fringe can be observed through the analysis of transmission electron microscopy (TEM) and high-resolution transmission electron microscopy (HRTEM) (Fig. 2a–c). Impressively, after the introduction of Mo atoms, the smooth surface of g-C₃N₄ still maintains as shown in atomic force microscopy (AFM) (Fig. S2a–b). All the above results demonstrate that no Mo particles can be detected, in other words, the Mo species are atomically dispersed as tiny clusters or single atoms on the g-C₃N₄ sheets. The atomically dispersed Mo can be confirmed by aberration-corrected high-angle annular dark field scanning transmission electron microscopy (HAADF-STEM) as shown in Figs. 2d and S2c–d. The bright spots with the size of about 0.16 nm are corresponding to single Mo atoms which are homogeneously distributed

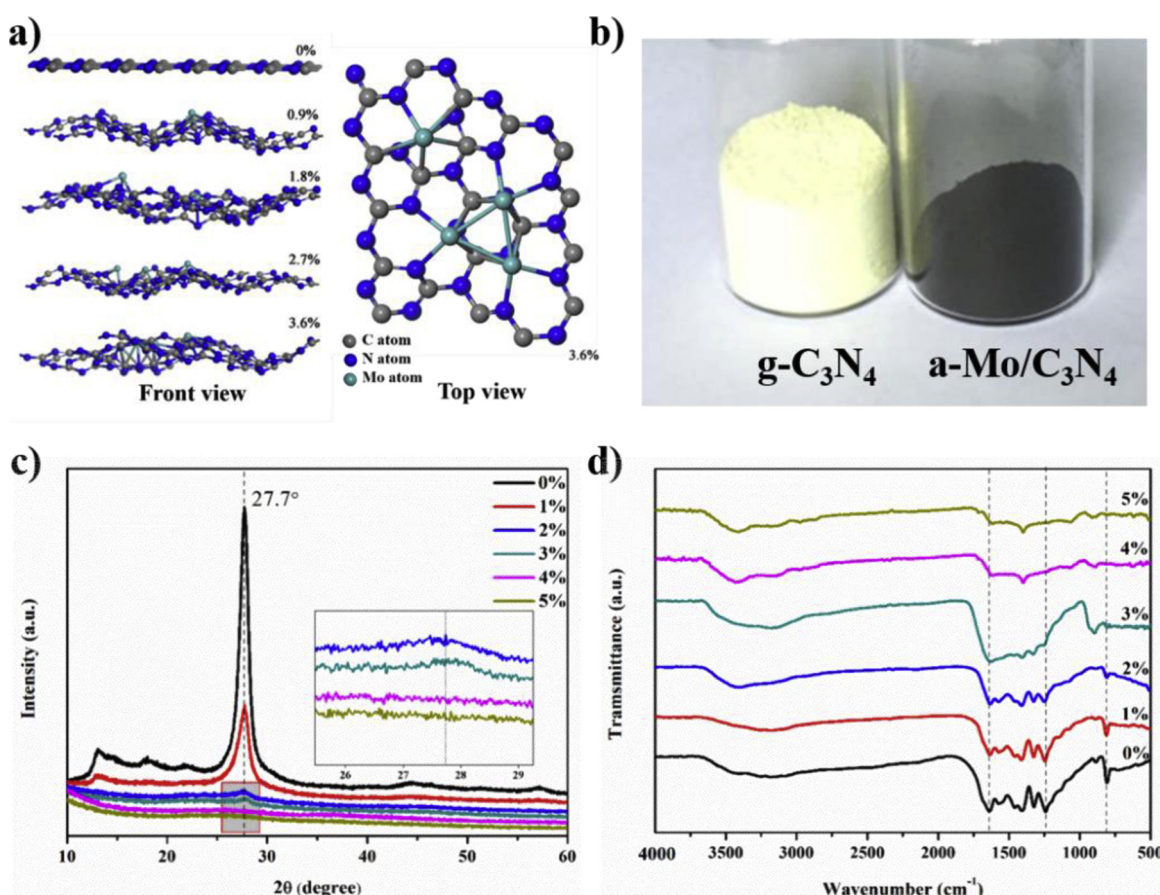


Fig. 1. (a) The optimized structure of (0–4%) Mo atoms on g-C₃N₄ surface; (b) Color of g-C₃N₄ and a-Mo/C₃N₄-4%; (c) Comparison of XRD patterns and (d) FTIR spectra of g-C₃N₄ (0%) and Mo/C₃N₄ (1–5%).

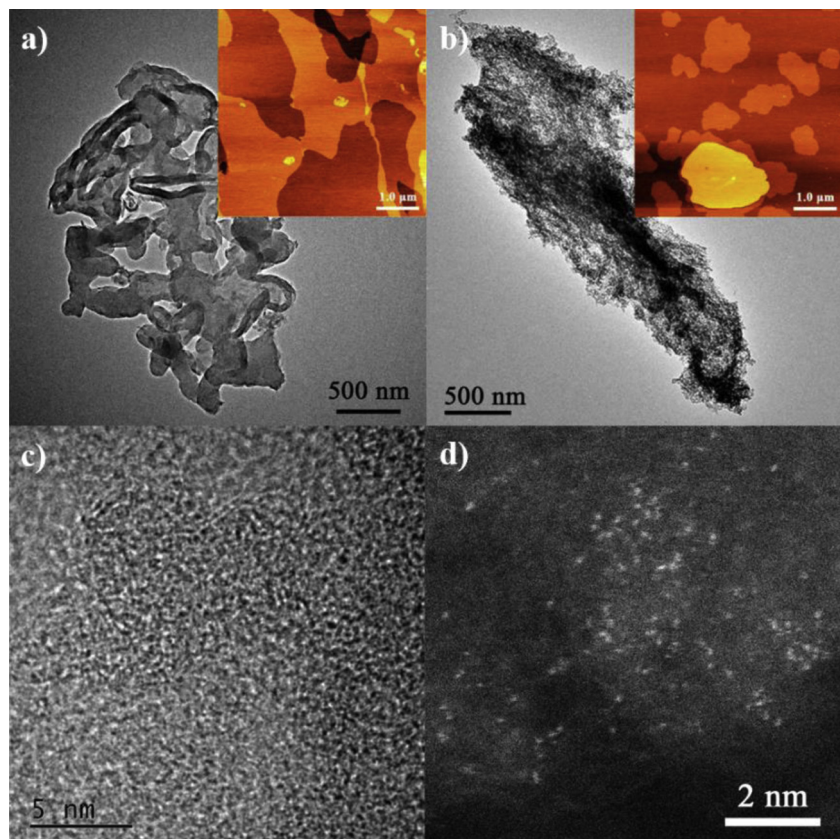


Fig. 2. TEM image of pure $\text{g-C}_3\text{N}_4$ (a) and $\text{a-Mo/C}_3\text{N}_4$ (b) (insert: AFM image); HRTEM (c) and HAADF-STEM (d) of $\text{a-Mo/C}_3\text{N}_4$.

across the $\text{g-C}_3\text{N}_4$ nanosheets. In addition, some tiny clusters organized by several Mo atoms can also be observed (Fig. 2d). The above results reveal that the Mo atom was atomically dispersed on $\text{g-C}_3\text{N}_4$ and the introduction of Mo causes the amorphous transformation of $\text{g-C}_3\text{N}_4$. Interestingly, this amorphous transformation only occurred when the Mo atoms were introduced during the formation of $\text{g-C}_3\text{N}_4$. Once the crystallization of $\text{g-C}_3\text{N}_4$ was achieved, the introduction of Mo species no longer causes the amorphous transformation as demonstrated in Fig. S3 (Particle Mo/ C_3N_4 is yellow-grey which is different from the black amorphous Mo/ C_3N_4).

3.2. Photocatalytic CO_2 reduction

Photocatalytic conversion of CO_2 was performed to investigate the

photocatalytic activity. As depicted in Fig. 3a–b, under visible light illumination for 6 h, pure $\text{g-C}_3\text{N}_4$ possesses a low CO and H_2 evolution of 10 and 56 $\mu\text{mol g}^{-1}$ while the highest CO and H_2 production of 105 and 224 $\mu\text{mol g}^{-1}$ are recorded for $\text{a-Mo/C}_3\text{N}_4$ (4%), which manifests a remarkable 10.6- and 4.0-fold enhancement of that over crystalline $\text{g-C}_3\text{N}_4$, respectively. Impressively, the achieved CO production over $\text{a-Mo/C}_3\text{N}_4$ (4%) is higher than that of previously reported $\text{g-C}_3\text{N}_4$ based photocatalyst as presented in Table S2 [31–35] and particle Mo/ C_3N_4 ($2.1 \mu\text{mol g}^{-1} \text{ h}^{-1}$, Fig. S4b), suggesting the superior photocatalytic activity for CO_2 reduction of $\text{a-Mo/C}_3\text{N}_4$. In addition, the CO selectivity between CO and CH_4 is as high as 99.3% (Fig. S4), which should be due to the significantly decreased energy barriers for CO_2 reduction to CO as demonstrated in the previous theoretical calculation [36] and the highest energy barrier of 3.53 eV for the hydrogenation of CO^*

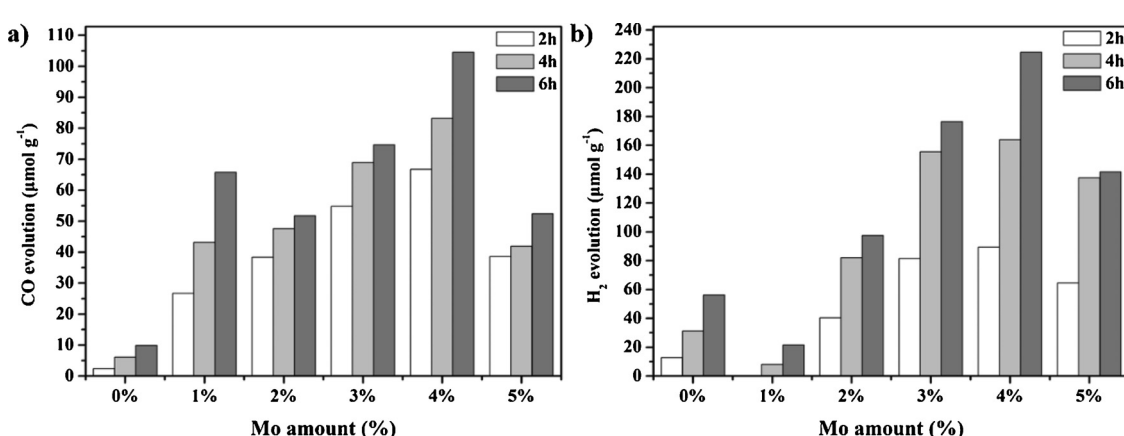


Fig. 3. Production of CO (a) and H_2 (b) over $\text{g-C}_3\text{N}_4$ (0%) and $\text{a-Mo/C}_3\text{N}_4$ (1%–5%). Conditions: catalyst (50 mg); CO_2 (99.999%); 20 mL water; 300 W Xe lamp light source with a cut-off filter ($\lambda > 420 \text{ nm}$).

according to the density functional theory (DFT) calculations (Fig. S5).

3.3. Photocatalytic mechanism

Typically, there are three main determined factors for the photocatalytic performance: (I) solar light absorption; (II) charge carriers transfer; (III) surface reaction [37–39]. Crystalline-C₃N₄ (pure g-C₃N₄), hemicrystalline-C₃N₄ (a-Mo/C₃N₄-1%) and amorphous-C₃N₄ (a-Mo/C₃N₄-4%) are selected for investigating the mechanism of enhanced photocatalytic performance. Specific surface area (SSA) can influence the adsorption of pollutant and the photocatalytic active sites, thus affecting the surface reaction [40]. The introduction of Mo atoms significantly enlarges the surface area from 13.2 to 61.2, 71.3, 66.9, 63.9 and 59.5 m² g⁻¹ with the increased amount of Mo (Fig. S6 and Table S3), which improve the surface CO₂ absorption and visible light absorption owing the scattering induced multiple internal reflection inside the hierarchical structures, leading to the enhanced photocatalytic activity. However, the order of surface area of Mo/C₃N₄ is not in accordance with the order of photocatalytic activity, implying that the specific surface is not the determined factor for photoreduction CO₂ over these samples.

The bandgap of semiconductor determines light absorption [41]. As shown in Fig. 4a, total and partial density of states (PDOS) reveal that with increasing the amount of Mo atoms, the bandgap of g-C₃N₄ (2.7 eV) is red shift to 2.0, 1.6, 1.6 and 0.9 eV. A new orbital originated from Mo 4d orbital is appeared near the Fermi level and becomes the main composition of the top of VB. This narrowed bandgap is attributed to not only the lattice distortion but also the formation of impurity energy level caused by Mo 4d orbital. As a proof, UV-vis diffuse reflection spectra (DRS) were performed (Figs. 4b and S7). Pure g-C₃N₄ possesses an absorption edge at about 445 nm corresponding to a bandgap of 2.69 eV, while strong band tails can be observed at the whole visible-light range after the introduction of atomically dispersed Mo, which originate from the amorphous transformation and result in narrowed bandgaps of 2.57, 1.63, 1.55 and 1.54 eV, respectively. These results are in accordance with the theoretical electronic band structures displayed above. Particularly, despite the bandgap of g-C₃N₄ has been significantly narrowed after the introduction of Mo, it still meets the thermodynamic requirements of the redox potentials of CO₂/CO (-0.53 V vs NHE) and H⁺/H₂ (-0.24 V vs NHE) as shown in the band structure diagram (Fig. S8).

Another important factor affects the photocatalytic ability is the

separation efficiency of photogenerated electron-hole pairs. Fig. 4c displays the photoluminescence (PL) spectra of pure g-C₃N₄ and a-Mo/C₃N₄. Obviously, pure g-C₃N₄ possesses the highest PL intensity, indicating its rapid recombination of photogenerated charge carriers originated from the high delocalization conjugate structure, while the introduction of atomically dispersed Mo remarkably decreases the PL intensity and a-Mo/C₃N₄-4% has almost no PL peak, demonstrating the high separation efficiency of charge carriers. Interestingly, time-resolved transient PL decay spectra reveal that after coupling with atomically dispersed Mo, the PL lifetime of g-C₃N₄ reduces from 4.4 ns to 3.6 and 2.5 ns (a-Mo/C₃N₄-1% and 4%), respectively, suggesting that the introduction of atomically dispersed Mo significantly accelerates the transfer of electrons (Fig. 4d) [42]. Moreover, a-Mo/C₃N₄ (4%) also represents the highest photocurrent and the lowest impedance as shown in the time-dependent photocurrent curves (i-t curve) and electrochemical impedance spectroscopy (EIS) (Fig. S9), demonstrating its high-efficiency of charge separation and transfer. Therefore, the introduction of atomically dispersed Mo has significantly increased the transfer of charge carriers.

Theoretically, owing to the lack of long-range order structure, amorphous materials usually possess rapid recombination of photogenerated electron-hole pairs. However, our current work is not the case. In order to further investigate the reason of enhanced separation efficiency, electron localization function (ELF) was calculated and displayed in Fig. 4e. It can be clearly seen that as the amount of Mo atoms increases, new Mo–C and Mo–N bonds appear and the electrons become even more highly localized around Mo atoms. It has been widely reported that the formation of new bonds can provide new electron and hole transport pathways to hinder the recombination of charge carriers [43–45]. In our system, according to the analysis of PDOS, after the introduction of Mo atoms, a new Mo 4d orbital appears in both CB and VB energy region. Thus, the Mo–N bond is described by the Mo 4d–N 2p overlap in the energy region of VB, but the Mo–C bond is described by the Mo 4d–C 2p overlap in the energy region of CB. Therefore, photogenerated electrons and holes could transfer through the new Mo–C and Mo–N bonds, respectively, accelerating the separation of charge carriers.

To investigate the formation of new bonds, the electronic and local structures of Mo were performed by X-ray absorption fine structure (XAFS). As shown in the X-ray absorption near-edge structure (XANES) spectra and the correlation between Mo K-edge half-step energy and oxidation state (Figs. 5a and S10a), the characteristic features of 1%

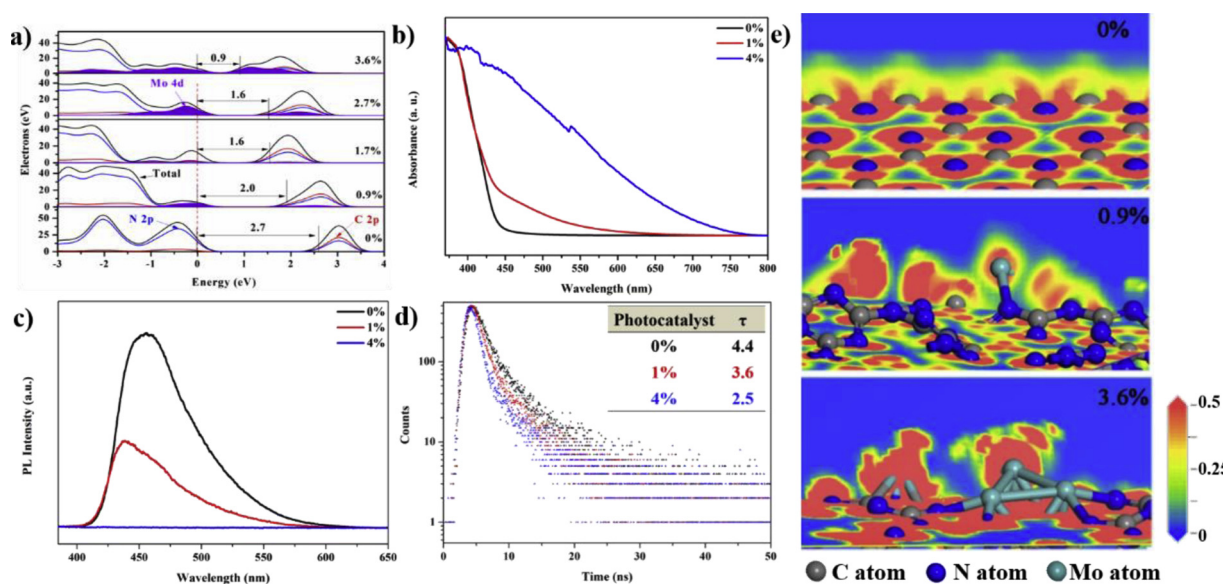


Fig. 4. (a) DOS of different Mo/C₃N₄; UV-vis (b), PL (c), time-resolved PL spectra (d) and ELF (e) of g-C₃N₄ (0%) and a-Mo/C₃N₄ (1% and 4%).

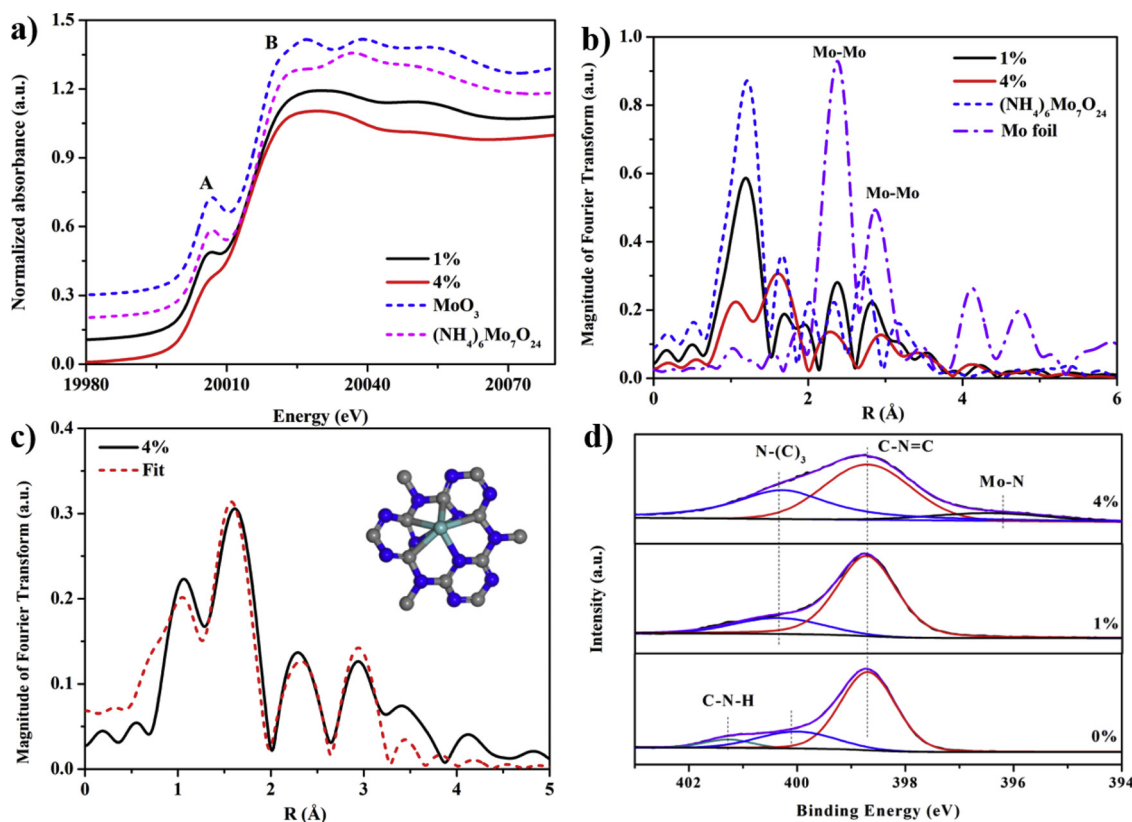


Fig. 5. (a)XANES spectra at the Mo K edge for a-Mo/C₃N₄ (1 and 4%), standard MoO₃ and standard (NH₄)₆Mo₇O₂₄; K²-weighted EXAFS Fourier transform (FT) magnitudes of the Mo K edge (b) and fitting of 4% sample (c). (d) High-resolution N 1s XPS spectra.

and 4% samples are quite different (labelled feature A and B in Fig. 5a): the state of Mo in the 1% sample is close to MoO₃ revealing the main state of Mo is Mo (VI), which becomes Mo (IV) for 4% sample due to the electron localization around Mo atom as indicated in ELF (Fig. 4e). Fig. S10b shows the XANES simulation of DFT-calculated 4% sample. Mo atoms have four different oxidation states based on its position. Mo1 has the highest oxidation state while the oxidation states of Mo2, Mo3 and Mo4 gradually decrease. It should be noted that the XANES of Mo4 is close to that of as-prepared 4% sample, demonstrating that the tiny clusters are most in the 4% sample, which lead to the amorphous transformation of g-C₃N₄. Figs. 5b, c and S10 c, d display the extended X-ray absorption fine structure (FT-EXAFS) spectra of a-Mo/C₃N₄ in k-space and corresponding FT spectra in R-space with their fitting parameters summarized in Table S4. Obviously, the relative mean-square displacement (MSD, σ^2) becomes large as the increasing amount of Mo atoms, indicating the increased disorder of structure and thus further confirming the phase transformation from crystalline to amorphous. Moreover, it should be noted that the Mo–Mo bonds with less coordination number (CN) demonstrate the presence of tiny clusters in accord with the HAADF-STEM image. Importantly, a new bond corresponding to Mo–C bond can be observed for a-Mo/C₃N₄ (4%). However, owing to the similar bond length of Mo–N and Mo–O and the certain existence of Mo–O bond originated from the ammonium molybdate, these two bonds are not clearly separated in the fitting process. Fig. 5d demonstrates the high-resolution X-ray photoelectron spectroscopy (XPS) spectra of N 1s. The peak of g-C₃N₄ at 398.7 eV is ascribed to C–N–C bond while the peak at 400.1 eV is assigned to the N–(C)₃ bond [28]. In particular, the peak at 401.3 eV corresponding to C–N–H bond is disappeared after the introduction of Mo atoms, further confirming the broken of hydrogen bonds between strands of polymeric melon units [46,47]. Interestingly, a new peak at 396.2 eV can be observed for a-Mo/C₃N₄, which is originated from the Mo–N bond, proving the formation of Mo–N bond after the introduction of

Mo atoms [48]. These results confirm the formation of new Mo–C and Mo–N bonds, which provide new electrons and holes transport pathways to accelerate the separation of charge carriers.

On the base of the above discussions, a possible photocatalytic reduction of CO₂ mechanism over a-Mo/C₃N₄ was delineated in Fig. 6. Typically, there are three main steps: (I) CO₂ adsorption; (II) electrons excitation and transfer; (III) surface reaction. For pure g-C₃N₄, its small surface area, low light absorption, rapid recombination of charge carriers as well as high reaction barriers significantly limits its photocatalytic activity. After the introduction of atomically dispersed Mo, the insert of Mo atoms into the structure of g-C₃N₄ causes a distorted lattice and disordered atomic arrangement, thus resulting in a phase transition from crystalline to amorphous. This amorphous transformation significantly enlarges the surface area from 13.2 to 61.2 – 71.3 m²g⁻¹ and gives a strong tail in the range of visible light, enhancing CO₂ adsorption and visible-light absorption. Moreover, the introduction of atomically dispersed Mo creates new Mo–C and Mo–N bonds, which provide new electrons and holes transport pathways to accelerate the separation of photogenerated electron-hole pairs. Furthermore, the

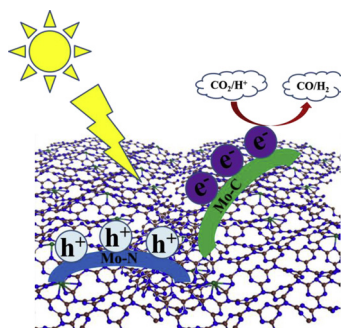


Fig. 6. Schematic illustration of CO₂ photoreduction over a-Mo/C₃N₄.

introduction of Mo atoms as the active sites can significantly decrease the energy barriers for CO₂ reduction as demonstrated in previous theoretical calculation [36].

4. Conclusion

In summary, we found the atomically dispersed Mo atoms can be formed on g-C₃N₄ and induce the amorphous transformation of g-C₃N₄. In this case, the strong interfacial interaction between Mo atoms and g-C₃N₄ significantly destroyed the long order structure of g-C₃N₄, resulting in the phase transition from crystalline to amorphous. This amorphous transformation significantly enhanced the visible light absorption originated from the strong band tail and remarkably enhanced the absorbance edge up to 750 nm. Meanwhile, the new formed Mo—C and Mo—N bonds provide new electrons and holes transport pathways to accelerate the separation of photoexcited electron-hole pairs. As a result, the obtained a-Mo/C₃N₄ possesses outstanding photoreduction CO₂ activity with CO and H₂ production rate of 18 and 37 μmol g⁻¹ h⁻¹ under visible light illumination, which is 10.6- and 4-folds enhancement over crystalline g-C₃N₄. This work provides a fresh concept to fabricate high-efficient amorphous photocatalyst induced by atomically dispersed metal atoms.

Acknowledgements

We gratefully acknowledge financial support from the Sichuan Provincial International Cooperation Project (2017HH0030), the Innovative Research Team of Sichuan Province (2016TD0011), the National Natural Science Foundation of China (No. 51872147) and the Program for Innovative Research Team of Science and Technology in the University of Henan Province (19IRTSTHN025). We thank Shanghai Synchrotron Radiation Facility (SSRF) for beamtime at BL14W1 line and Prof. Kunhao Zhang at SSRF for his kind help. Ruiyang Zhang and Penghui Li contributed equally to this work. We appreciate the calculations support from the National Supercomputing Center in Shenzhen.

Appendix A. Supplementary data

Supplementary material related to this article can be found, in the online version, at doi:<https://doi.org/10.1016/j.apcatb.2019.03.025>.

References

- [1] A. Fujishima, K. Honda, *Nature* 238 (1972) 37.
- [2] R. Asahi, T. Morikawa, T. Ohwaki, K. Aoki, Y. Taga, *Science* 293 (2001) 269–271.
- [3] A.L. Linsebigler, G. Lu, J.T. Yates, *Chem. Rev.* 95 (1995) 735–758.
- [4] L. Yuliati, H. Yoshida, *Chem. Soc. Rev.* 37 (2008) 1592–1602.
- [5] H. Yoshida, L. Zhang, M. Sato, T. Morikawa, T. Kajino, T. Sekito, S. Matsumoto, H. Hirata, *Catal. Today* 251 (2015) 132–139.
- [6] M. Yamamoto, T. Yoshida, N. Yamamoto, T. Nomoto, Y. Yamamoto, S. Yagi, H. Yoshida, *J. Mater. Chem. A* 3 (2015) 16810–16816.
- [7] Q. Xiang, J. Yu, M. Jaroniec, *Chem. Soc. Rev.* 41 (2012) 782–796.
- [8] Y. Wang, R. Shi, J. Lin, Y. Zhu, *Energy Environ. Sci.* 4 (2011) 2922–2929.
- [9] Y. Kang, Y. Yang, L.C. Yin, X. Kang, G. Liu, H.M. Cheng, *Adv. Mater.* 27 (2015) 4572–4577.
- [10] X. Chen, L. Liu, P.Y. Yu, S.S. Mao, *Science* 331 (2011) 746–750.
- [11] B. Ohtani, Y. Ogawa, S. Nishimoto, *J. Phys. Chem. B* 101 (1997) 3746–3752.
- [12] S. Hu, M.R. Shaner, J.A. Beardslee, M. Licherman, B.S. Brunschwig, N.S. Lewis, *Science* 344 (2014) 1005–1009.
- [13] Y. Li, T. Sasaki, Y. Shimizu, N. Koshizaki, *J. Am. Chem. Soc.* 130 (2008) 14755–14762.
- [14] L. Zhang, P.F. Liu, Y.H. Li, C.W. Wang, M.Y. Zu, H.Q. Fu, X.H. Yang, H.G. Yang, *ACS Catal.* 8 (2018) 5200–5205.
- [15] M.Z. Rahman, P.C. Tapping, T.W. Kee, R. Smernik, N. Spooner, J. Moffatt, Y. Tang, K. Davey, S.Z. Qiao, *Adv. Funct. Mater.* 27 (2017) 1702384.
- [16] B. Qiao, A. Wang, X. Yang, L.F. Allard, Z. Jiang, Y. Cui, J. Liu, J. Li, T. Zhang, *Nat. Chem.* 3 (2011) 634–641.
- [17] X. Cui, W. Li, P. Ryabchuk, K. Junge, M. Beller, *Nat. Catal.* 1 (2018) 385–397.
- [18] L. Wang, H. Li, W. Zhang, X. Zhao, J. Qiu, A. Li, X. Zheng, Z. Hu, R. Si, J. Zeng, *Angew. Chem. Int. Ed.* 56 (2017) 4712–4718.
- [19] H.B. Yang, S.F. Hung, S. Liu, K. Yuan, S. Miao, L. Zhang, X. Huang, H.Y. Wang, W. Cai, R. Chen, J. Gao, X. Yang, W. Chen, Y. Huang, H.M. Chen, C.M. Li, T. Zhang, B. Liu, *Nat. Energy* 3 (2018) 140.
- [20] X. Zhao, S. Chen, Z. Fang, J. Ding, W. Sang, Y. Wang, J. Zhao, Z. Peng, J. Zeng, J. *Am. Chem. Soc.* 137 (2015) 2804–2807.
- [21] Y. Zhou, Z. Zhao, F. Wang, K. Cao, D.E. Doronkin, F. Dong, J.D. Grunwaldt, J. *Hazard. Mater.* 307 (2016) 163–172.
- [22] F. Wang, Y. Han, C.S. Lim, Y. Lu, J. Wang, J. Xu, H. Chen, C. Zhang, M. Hong, X. Liu, *Nature* 463 (2010) 1061–1065.
- [23] S.C. Erwin, L. Zu, M.I. Haftel, A.L. Efros, T.A. Kennedy, D.J. Norris, *Nature* 436 (2005) 91–94.
- [24] X. Wang, K. Maeda, A. Thomas, K. Takanabe, G. Xin, J.M. Carlsson, K. Domen, M. Antonietti, *Nat. Mater.* 8 (2009) 76–80.
- [25] W.J. Ong, L.L. Tan, Y.H. Ng, S.T. Yong, S.P. Chai, *Chem. Rev.* 116 (2016) 7159–7329.
- [26] R. Zhang, M. Ma, Q. Zhang, F. Dong, Y. Zhou, *Appl. Catal. B: Environ.* 235 (2018) 17–25.
- [27] S. Cao, J. Low, J. Yu, M. Jaroniec, *Adv. Mater.* 27 (2015) 2150–2176.
- [28] F. Dong, Z. Zhao, T. Xiong, Z. Ni, W. Zhang, Y. Sun, W.K. Ho, *ACS Appl. Mater. Interfaces* 5 (2013) 11392–11401.
- [29] W. Wan, S. Yu, F. Dong, Q. Zhang, Y. Zhou, *J. Mater. Chem. A* 4 (2016) 7823–7829.
- [30] W.J. Ong, L.L. Tan, S.P. Chai, S.T. Yong, A.R. Mohamed, *Nano Energy* 13 (2015) 757–770.
- [31] M. Li, L. Zhang, X. Fan, Y. Zhou, M. Wu, J. Shi, *J. Mater. Chem. A* 3 (2015) 5189–5196.
- [32] W.J. Ong, L.K. Putri, Y.C. Tan, L.L. Tan, N. Li, Y.H. Ng, X. Wen, S.P. Chai, *Nano Res.* 10 (2017) 1673–1696.
- [33] S. Liu, B. Weng, Z.R. Tang, Y.J. Xu, *Nanoscale* 7 (2015) 861–866.
- [34] S. Zhou, Y. Liu, J. Li, Y. Wang, G. Jiang, Z. Zhao, D. Wang, A. Duan, J. Liu, Y. Wei, *Appl. Catal. B: Environ.* 158 (2014) 20–29.
- [35] M. Li, L. Zhang, X. Fan, M. Wu, M. Wang, R. Cheng, L. Zhang, H. Yao, J. Shi, *Appl. Catal. B: Environ.* 201 (2017) 629–635.
- [36] P. Li, F. Wang, S. Wei, X. Li, Y. Zhou, *Phys. Chem. Chem. Phys.* 19 (2017) 4405–4410.
- [37] J. Schneider, M. Matsuoka, M. Takeuchi, J. Zhang, Y. Horiuchi, M. Anpo, D.W. Bahnemann, *Chem. Rev.* 114 (2014) 9919–9986.
- [38] D.M. Schultz, T.P. Yoon, *Science* 343 (2014) 1239176.
- [39] L.J. Fang, X.L. Wang, Y.H. Li, P.F. Liu, Y.L. Wang, H.D. Zeng, H.G. Yang, *Appl. Catal. B: Environ.* 200 (2017) 578–584.
- [40] T. Zhang, W. Lin, *Chem. Soc. Rev.* 43 (2014) 5982–5993.
- [41] S. Ghosh, N.A. Kouamé, L. Ramos, S. Remita, A. Dazzi, A. Deniset-Besseau, P. Beaunier, F. Goubard, P.H. Aubert, H. Remita, *Nat. Mater.* 14 (2015) 505–511.
- [42] S. Cao, H. Li, T. Tong, H.C. Chen, A. Yu, J. Yu, H.M. Chen, *Adv. Funct. Mater.* 28 (2018) 1802169.
- [43] L. Qian, J.F. Chen, Y.H. Li, L. Wu, H.F. Wang, A.P. Chen, P. Hu, L.R. Zheng, H.G. Yang, *Angew. Chem. Int. Ed.* 54 (2015) 11467–11471.
- [44] Y. Wu, P. Wang, X. Zhu, Q. Zhang, Z. Wang, Y. Liu, G. Zou, Y. Dai, M.H. Whangbo, B. Huang, *Adv. Mater.* 30 (2018) 1704342.
- [45] H. Li, L. Wang, Y. Dai, Z. Pu, Z. Lao, Y. Chen, M. Wang, X. Zheng, J. Zhu, W. Zhang, R. Si, C. Ma, J. Zeng, *Nat. Nanotechnol.* 13 (2018) 411–417.
- [46] X. Chen, L. Zhang, B. Zhang, X. Guo, X. Mu, *Sci. Rep.* 6 (2016) 28558.
- [47] F. He, G. Chen, Y. Yu, S. Hao, Y. Zhou, Y. Zheng, *ACS Appl. Mater. Interfaces* 6 (2014) 7171–7179.
- [48] M. Anpo, P.V. Kamat, *Environmentally Benign Photocatalysts: Applications of Titanium Oxide-Based Materials*, Springer Science & Business Media, 2010.